CrossMark

JM PAPERS

DNS of passive scalars in turbulent pipe flow

Sergio Pirozzoli[1,†], **Joshua Romero**[2], **Massimiliano Fatica**[2],
Roberto Verzicco[3,4] **and Paolo Orlandi**[1]

[1]Dipartimento di Ingegneria Meccanica e Aerospaziale, Sapienza Università di Roma, Via Eudossiana 18, 00184 Roma, Italy

[2]NVIDIA Corporation, 2701 San Tomas Expressway, Santa Clara, CA 95050, USA

[3]Dipartimento di Ingegneria Industriale, Università di Roma TorVergata, Via del Politecnico 1, 00133 Roma, Italy

[4]Physics of Fluid Group, University of Twente, P.O. Box 217, 7500 AE Enschede, The Netherlands

We study the statistics of passive scalars at $Pr = 1$, for turbulent flow within a smooth straight pipe of circular cross section up to $Re_\tau \approx 6000$ using direct numerical simulation (DNS) of the Navier–Stokes equations. While featuring a general organisation similar to the axial velocity field, passive scalar fields show additional energy at small wavenumbers, resulting in a higher degree of mixing and in a $k^{-4/3}$ spectral inertial range. The DNS results highlight logarithmic growth of the inner-scaled bulk and mean centreline scalar values with the friction Reynolds number, implying an estimated scalar von Kármán constant $k_\theta \approx 0.459$, which also nicely fits the mean scalar profiles. The DNS data are used to synthesise a modified form of the classical predictive formula of Kader & Yaglom (*Intl J. Heat Mass Transfer*, vol. 15 (12), 1972, pp. 2329–2351), which points to some shortcomings of the original formulation. Universality of the mean core scalar profile in defect form is recovered, with very nearly parabolic shape. Logarithmic growth of the buffer-layer peak of the scalar variance is found in the Reynolds number range under scrutiny, which well conforms with Townsend's attached-eddy hypothesis, whose validity is also supported by the spectral maps. The behaviour of the turbulent Prandtl number shows good universality in the outer wall layer, with values $Pr_t \approx 0.84$, as also found in previous studies, but closer to unity near the wall, where existing correlations do not reproduce the observed trends.

Key words: pipe flow, pipe flow boundary layer, turbulence simulation

† Email address for correspondence: sergio.pirozzoli@uniroma1.it

S. Pirozzoli, J. Romero, M. Fatica, R. Verzicco and P. Orlandi

1. Introduction

The study of passive scalars evolving within wall-bounded turbulent flows has great practical importance, being relevant for the behaviour of diluted contaminants and/or as a model for the temperature field under the assumption of low Mach number and small temperature differences (Monin & Yaglom 1971; Cebeci & Bradshaw 1984). It is well known that measurements of concentration of passive tracers and of small temperature differences are quite difficult and, in fact, available information about even basic passive scalar statistics are rather limited (Gowen & Smith 1967; Kader 1981; Subramanian & Antonia 1981; Nagano & Tagawa 1988), mostly including basic mean properties and overall mass or heat transfer coefficients. Although existing semi-empirical correlations have sufficient accuracy for engineering design (Kays, Crawford & Weigand 1980), their theoretical foundations are not firmly established. Furthermore, assumptions typically made in turbulence models such as constant turbulent Prandtl number are known to be crude approximations in the absence of reliable reference data.

Given this scenario, direct numerical simulation (DNS) is the natural candidate to establish a credible database for the physical analysis of passive scalars in wall turbulence, and for the development and validation of phenomenological prediction formulae and turbulence models. Most DNS studies of passive scalars in wall turbulence have been so far carried out for the prototype case of planar channel flow, starting with the work of Kim & Moin (1989), at $Re_\tau = 180$ (here $Re_\tau = u_\tau R/\nu$ is the friction Reynolds number, with $u_\tau = (\tau_w/\rho)^{1/2}$ the friction velocity, R the pipe radius, ν the fluid kinematic viscosity, ρ the fluid density and τ_w the wall shear stress), in which the forcing of the scalar field was achieved using a spatially and temporally uniform source term. Additional simulations at increasingly high Reynolds number were carried out by Kawamura, Abe & Matsuo (1999) and Abe, Kawamura & Matsuo (2004), based on enforcement of strictly constant heat flux in time (this approach is hereafter referred to as CHF), which first allowed scale separation effects to be appreciated and a reasonable value of the scalar von Kármán constant $k_\theta \approx 0.43$ to be deduced, as well as effects of Prandtl number variation (the molecular Prandtl number is here defined as the ratio of the kinematic viscosity to the scalar diffusivity, $Pr = \nu/\alpha$). Those studies showed close similarity between the streamwise velocity and passive scalar field in the near-wall region, as after the classical Reynolds analogy. Specifically, the scalar field was found to be organised into streaks whose size scales in wall units, with a correlation coefficient between streamwise velocity fluctuations and scalar fluctuations close to unit. Computationally high Reynolds numbers ($Re_\tau \approx 4000$, with $Pr \leq 1$) were reached in the study of Pirozzoli, Bernardini & Orlandi (2016), using spatially uniform forcing in such a way as to maintain the bulk temperature constant in time (this approach is hereafter referred to as CMT). Recent large-scale channel flow DNS with passive scalars using the CHF forcing at $Pr = 0.71$ (as representative of air) have been carried out by Alcántara-Ávila, Hoyas & Pérez-Quiles (2021).

Flow in a circular pipe is clearly more practically relevant than planar channel flow in view of applications such as heat exchangers, and it has been the subject of a number of experimental studies, mainly aimed at predicting the heat transfer coefficient as a function of the bulk flow Reynolds number (Kays *et al.* 1980). High-fidelity numerical simulations including passive scalars in pipe flow have been quite scarce so far and mainly include studies at $Re_\tau \leq 1000$ (Piller 2005; Redjem-Saad, Ould-Rouiss & Lauriat 2007; Saha *et al.* 2011; Antoranz *et al.* 2015; Straub *et al.* 2019). The current knowledge about gross properties and mean scalar profiles across the Reynolds and Prandtl numbers envelope thus currently rests on semi-empirical correlations (Kays *et al.* 1980; Kader 1981), which, although suitable for practical applications, deserve careful scrutiny. Clearly, the state of the art is not as well developed as for planar channel flow.
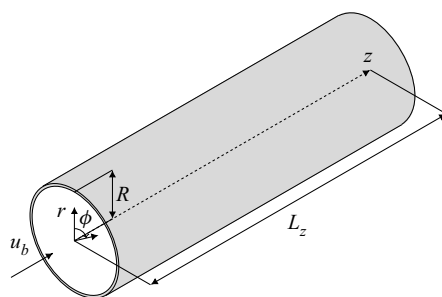
940 A45-2

Figure 1. Definition of the coordinate system for DNS of pipe flow, where z, r and ϕ are the axial, radial and azimuthal directions, respectively, R is the pipe radius, L_z the pipe length and u_b is the bulk velocity.

In this paper, we thus present DNS data of turbulent flow in a smooth circular pipe up to $Re_\tau \approx 6000$, including a passive scalar field with $Pr = 1$, at which some asymptotic high-Reynolds-number effects appear which were not observed in previous studies. Relying on the DNS database, we carry out an analysis of the structure of passive scalars in turbulent pipe flow, revisit current theoretical inferences and discuss implications about possible trends in the extreme-Reynolds-number regime. From a more engineering standpoint, we also revisit formulae for heat transfer prediction, as well as assumptions made in Reynolds-averaged Navier–Stokes (RANS) models for passive scalar turbulence. Although, as previously pointed out, the study of passive scalars is relevant in several contexts, the main field of application is heat transfer and, therefore, from now on we refer to the passive scalar field as the temperature field (denoted as T), and scalar fluxes will be interpreted as heat fluxes. Details on the velocity statistics from the present DNS database were reported in a separate publication (Pirozzoli *et al.* 2021).

2. Numerical dataset

Numerical simulations of fully developed turbulent flow in a circular pipe are carried out assuming periodic boundary conditions in the axial (z) and azimuthal (ϕ) directions, as shown in figure 1. The velocity field is controlled by two parameters, namely the bulk Reynolds number ($Re_b = 2Ru_b/\nu$, with u_b the bulk velocity namely averaged over the cross section), and the relative pipe length, L_z/R. The incompressible Navier–Stokes equations are supplemented with the transport equation for a passive scalar field (hence, buoyancy effects are disregarded), with the same diffusivity as the velocity field (hence, we assume $Pr = 1$) and with isothermal boundary conditions at the pipe wall ($r = R$). The passive scalar equation is forced through a time-varying, spatially uniform source term (CMT approach), in the interest of achieving complete similarity with the streamwise momentum equation, with the obvious exclusion of pressure. Although the total heat flux resulting from the CMT approach is not strictly constant in time, it oscillates around its mean value under statistically steady conditions. Differences of the results obtained with the CMT and CHF approaches have been described by Abe & Antonia (2017) and Alcántara-Ávila *et al.* (2021), which although generally small deserve some attention.

The computer code used for the DNS is the spin-off of an existing solver previously used to study Rayleigh–Bénard convection in cylindrical containers at extreme Rayleigh numbers (Stevens *et al.* 2013). That code is, in turn, the evolution of the solver originally developed by Verzicco & Orlandi (1996), and used for DNS of pipe flow by Orlandi & Fatica (1997). A second-order finite-difference discretisation of the incompressible

Navier–Stokes equations in cylindrical coordinates is used, based on the classical marker-and-cell method (Harlow & Welch 1965), whereby pressure and passive scalars are located at the cell centres, whereas the velocity components are located at the cell faces, thus removing odd–even decoupling phenomena and guaranteeing discrete conservation of the total kinetic energy and passive scalar variance in the inviscid limit. The Poisson equation resulting from enforcement of the divergence-free condition is efficiently solved by double trigonometric expansion in the periodic axial and azimuthal directions, and inversion of tridiagonal matrices in the radial direction (Kim & Moin 1985). An extensive series of previous studies about wall-bounded flows from this group proved that second-order finite-difference discretisation yields in practical cases of wall-bounded turbulence results which are by no means inferior in quality to those of pseudo-spectral methods (e.g. Moin & Verzicco 2016; Pirozzoli *et al.* 2016). A crucial issue is the proper treatment of the polar singularity at the pipe axis. A detailed description of the subject is reported in Verzicco & Orlandi (1996), but, basically, the radial velocity u_r in the governing equations is replaced by $q_r = r u_r$ (r is the radial space coordinate), which by construction vanishes at the axis. The governing equations are advanced in time by means of a hybrid third-order low-storage Runge–Kutta algorithm, whereby the diffusive terms are handled implicitly, and convective terms in the axial and radial direction explicitly. An important issue in this respect is the convective time step limitation in the azimuthal direction, due to intrinsic shrinking of the cells size toward the pipe axis. To alleviate this limitation, we use implicit treatment of the convective terms in the azimuthal direction (Akselvoll & Moin 1996; Wu & Moin 2008), which enables marching in time with similar time step as in planar domains flow in practical computations. In order to minimise numerical errors associated with implicit time stepping, explicit and implicit discretisations of the azimuthal convective terms are linearly blended with the radial coordinate, in such a way that near the pipe wall the treatment is fully explicit, and near the pipe axis it is fully implicit. The code was adapted to run on clusters of graphic accelerators (GPUs), using a combination of CUDA Fortran and OpenACC directives, and relying on the CUFFT libraries for efficient execution of fast Fourier transforms (FFTs) (Ruetsch & Fatica 2014).

From now on, inner normalisation of the flow properties will be denoted with the '+' superscript, whereby velocities are scaled by u_τ, wall distances by ν/u_τ and temperatures with respect to the friction temperature,

$$T_\tau = \frac{\alpha}{u_\tau} \left\langle \frac{\mathrm{d}T}{\mathrm{d}y} \right\rangle_w. \tag{2.1}$$

In particular, the inner-scaled temperature is defined as $\theta^+ = (T - T_w)/T_\tau$, where T is the local temperature and T_w is the wall temperature. Capital letters are used to denote flow properties averaged in the homogeneous spatial directions and in time, brackets to denote the averaging operator and lowercase letters to denote fluctuations from the mean. Finally, bulk values of axial velocity and temperature are defined as

$$u_b = 2 \int_0^R r \langle u_z \rangle \, \mathrm{d}r \Big/ R^2, \quad T_b = 2 \int_0^R r \langle T \rangle \, \mathrm{d}r \Big/ R^2. \tag{2.2a,b}$$

A list of the main simulations that we have carried out is given in table 1. The mesh resolution is designed based on the criteria discussed by Pirozzoli & Orlandi (2021). In particular, the collocation points are distributed in the wall-normal direction so that approximately 30 points are placed within $y^+ \leq 40$ ($y = R - r$ is the wall distance), with the first grid point at $y^+ < 0.1$, and the mesh is progressively stretched in the

Dataset	L_z/R	Mesh ($N_z \times N_r \times N_\phi$)	Re_b	Nu	Re_τ	$\Delta t_{stat}/\tau_t$	Line colour
DNS-A	15	$256 \times 67 \times 256$	5300	24.8251	180.3	204.0	▬
DNS-B	15	$768 \times 140 \times 768$	17 000	60.2341	495.3	87.4	▬
DNS-C	15	$1792 \times 270 \times 1792$	44 000	124.178	1136.6	25.9	▬
DNS-C-SH	7.5	$1792 \times 270 \times 986$	44 000	124.098	1144.2	31.1	NA
DNS-C-LO	30	$1792 \times 270 \times 3944$	44 000	123.958	1134.6	24.5	NA
DNS-C-FF	15	$3944 \times 270 \times 1792$	44 000	123.569	1131.0	31.3	NA
DNS-C-FR	15	$1792 \times 540 \times 1792$	44 000	124.625	1135.7	28.6	NA
DNS-C-FZ	15	$1792 \times 270 \times 3944$	44 000	122.196	1135.7	15.5	NA
DNS-D	15	$3072 \times 399 \times 3072$	82 500	202.662	1976.0	22.4	▬
DNS-E	15	$4608 \times 540 \times 4608$	133 000	296.485	3028.1	16.6	▬
DNS-F	15	$9216 \times 910 \times 9216$	285 000	539.975	6019.4	8.32	▬

Table 1. Flow parameters for DNS of pipe flow. Cases are labelled in increasing order of Reynolds number, from A to F. Suffixes SH and LO indicate DNS in short and long domains, respectively; FF, FR and FZ denote refinement along the ϕ, r and z directions, respectively.

outer wall layer in such a way that the mesh spacing is proportional to the local Kolmogorov length scale, which there varies as $\eta^+ \approx 0.8 y^{+1/4}$ (Jiménez 2018). Regarding the axial and azimuthal directions, finite-difference simulations of wall-bounded flows yield grid-independent results as long as $\Delta x^+ \approx 10$, $R^+ \Delta \phi \approx 4.5$ (Pirozzoli *et al.* 2016), hence we have selected the number of grid points along the homogeneous flow directions as $N_z = L_z/R \times Re_\tau/9.8$, $N_\phi \sim 2\pi \times Re_\tau/4.1$. According to the established practice (Hoyas & Jiménez 2006; Ahn *et al.* 2015; Lee & Moser 2015), the time intervals used to collect the flow statistics (Δt_{stat}) are reported as a fraction of the eddy-turnover time (R/u_τ).

The sampling errors for some key properties discussed in this paper have been estimated using the method of Russo & Luchini (2017), based on extension of the classical batch means approach. The results of the uncertainty estimation analysis are listed in table 2, where we provide expected values and associated standard deviations for the Nusselt number (Nu), mean temperature at the pipe centreline (Θ_{CL}^+) and peak temperature variance and its wall distance ($\langle \theta^2 \rangle_{IP}^+$ and y_{IP}^+, respectively). We find that the sampling error is generally quite limited, being larger in the largest DNS, which have been run for shorter time. In particular, in DNS-F, the expected sampling error in Nusselt number, centreline temperature and peak temperature variance is approximately 0.5 %. Additional tests aimed at establishing the effect of axial domain length and grid size have been carried out for the DNS-C flow case, whose results are also reported in table 2. We find that even halving the pipe length yields minimal change in the basic flow properties, which is well within the uncertainty bounds. This is in contrast to properties related to the velocity field, which are significantly affected from use of a short domain (Pirozzoli *et al.* 2021). The interesting consequence of this observation is the possibility to carry out DNS of scalar fields in more limited domains, as also noted by Alcántara-Ávila *et al.* (2021). In order to quantify uncertainties associated with numerical discretisation, additional simulations have been carried out by doubling the number of grid points in the azimuthal, radial and axial directions, respectively. Based on the data reported in the table, after discarding the short-pipe case, we can thus quantify the uncertainty due to numerical discretisation and limited pipe length to be approximately 0.2 % for the Nusselt number, 0.4 % for the pipe centreline temperature and 0.7 % for the peak temperature variance.

Dataset	Nu	Θ_{CL}^+	$\langle\theta^2\rangle_{IP}^+$	y_{IP}^+
DNS-A	$24.8251 \pm 0.16\,\%$	$18.31 \pm 0.054\,\%$	$7.667 \pm 0.24\,\%$	$15.40 \pm 0.24\,\%$
DNS-B	$60.2341 \pm 0.072\,\%$	$19.86 \pm 0.099\,\%$	$7.988 \pm 0.11\,\%$	$14.69 \pm 0.29\,\%$
DNS-C	$124.178 \pm 0.11\,\%$	$21.83 \pm 0.083\,\%$	$8.668 \pm 0.18\,\%$	$14.93 \pm 0.064\,\%$
DNS-C-SH	$124.098 \pm 0.11\,\%$	$22.21 \pm 0.091\,\%$	$8.760 \pm 0.28\,\%$	$14.89 \pm 0.082\,\%$
DNS-C-LO	$123.958 \pm 0.12\,\%$	$21.84 \pm 0.093\,\%$	$8.636 \pm 0.26\,\%$	$14.88 \pm 0.048\,\%$
DNS-C-FF	$123.569 \pm 0.12\,\%$	$21.89 \pm 0.12\,\%$	$8.591 \pm 0.18\,\%$	$14.88 \pm 0.053\,\%$
DNS-C-FR	$124.625 \pm 0.18\,\%$	$21.79 \pm 0.079\,\%$	$8.537 \pm 0.22\,\%$	$14.62 \pm 0.074\,\%$
DNS-C-FZ	$122.196 \pm 0.16\,\%$	$22.25 \pm 0.10\,\%$	$9.011 \pm 0.25\,\%$	$15.40 \pm 0.10\,\%$
DNS-D	$202.662 \pm 0.19\,\%$	$23.12 \pm 0.19\,\%$	$9.034 \pm 0.32\,\%$	$15.00 \pm 0.068\,\%$
DNS-E	$296.485 \pm 0.26\,\%$	$23.96 \pm 0.16\,\%$	$9.326 \pm 0.42\,\%$	$15.05 \pm 0.13\,\%$
DNS-F	$539.975 \pm 0.32\,\%$	$25.37 \pm 0.23\,\%$	$9.794 \pm 0.60\,\%$	$15.30 \pm 0.17\,\%$

Table 2. Uncertainty estimation study: mean values of representative quantities and standard deviation of their estimates, where Nu is the Nusselt number, Θ_{CL}^+ is the mean pipe centreline temperature, $\langle\theta_z^2\rangle_{IP}^+$ is the peak temperature variance and y_{IP}^+ is its distance from the wall.

3. Results

3.1. *General organisation of the temperature field*

Qualitative information about the structure of the flow field is provided by instantaneous perspective views of the axial velocity and temperature fields, which we show in figure 2. Although finer-scale details are visible at the higher Re_b, the flow in the cross-stream planes is always characterised by a limited number of bulges distributed along the azimuthal direction, which correspond to alternating intrusions of high-speed fluid from the pipe core and ejections of low-speed fluid from the wall. Streaks are visible in the near-wall cylindrical shells, whose organisation has clear association with the cross-stream pattern. Specifically, R-sized low-speed streaks are observed in association with large-scale ejections, whereas R-sized high-speed streaks occur in the presence of large-scale inrush from the core flow. At the same time, smaller streaks scaling in wall units appear, corresponding to buffer-layer ejections/sweeps. Hence, organisation of the flow on at least two length scales is apparent here, whose separation increases with Re_τ. As figure 2 shows, the temperature field has the same qualitative organisation as axial velocity, and low-speed streaks correspond to low-temperature thermal streaks. This is not surprising, given the formal similarity of the controlling equations at $Pr = 1$, and close association of the two quantities pointed out in many previous studies (e.g. Abe & Antonia 2009; Pirozzoli *et al.* 2016; Alcántara-Ávila, Hoyas & Pérez-Quiles 2018). It is interesting that this association includes both the large flow scales in the pipe core and the small, near-wall streaks. Zooming in closer (see figure 3), one can nevertheless detect some differences between the two fields, in that temperature tends to form sharper fronts, whereas the axial velocity field tends to be more blurred. As noted by Pirozzoli *et al.* (2016), this is due to the fact that the axial velocity is not passively advected, but rather it can react to the formation of fronts through feedback pressure. As a result, whereas the organisation at large scales is similar, smaller features are found in the temperature fields, as clearly highlighted in the corresponding spectral densities.

The spectral maps of u_z and θ are depicted in figure 4, for the DNS-F flow case. In order to isolate changes in the typical length scales, in the figure we show the azimuthal spectral densities normalised by the respective variances, defined as

$$\hat{E}_x(k_\phi) = E_x(k_\phi)/\langle x^2 \rangle, \tag{3.1}$$

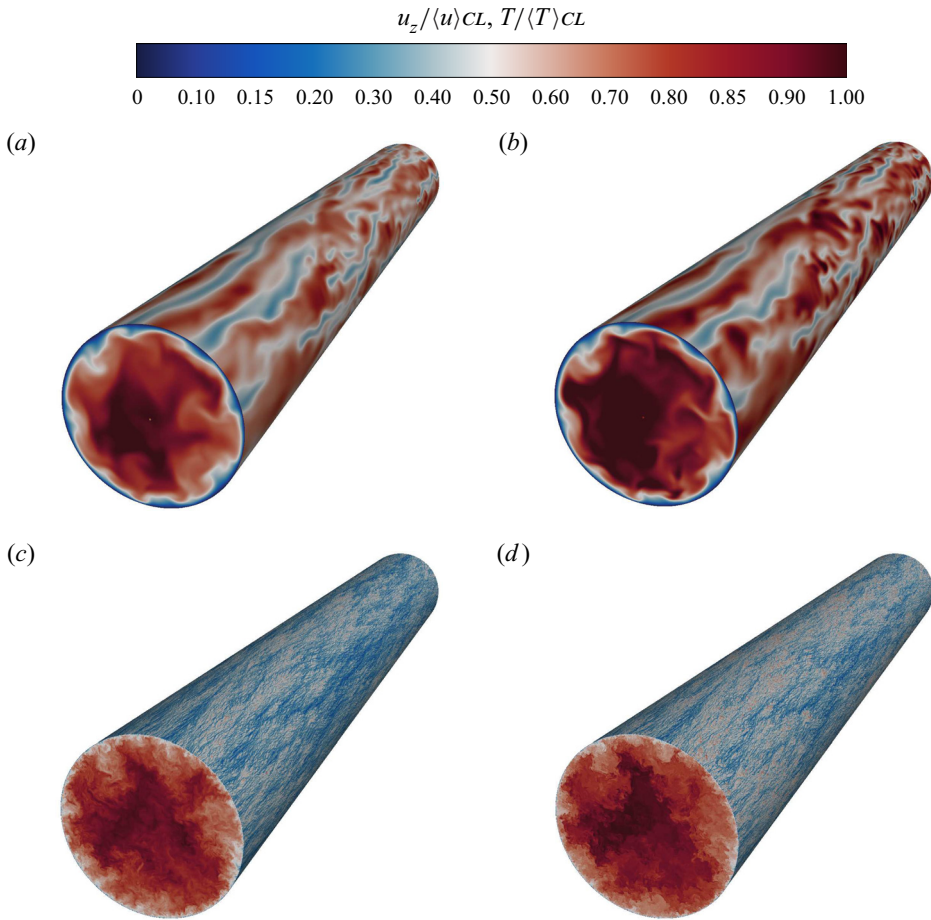$$u_z/\langle u \rangle_{CL}, T/\langle T \rangle_{CL}$$

Figure 2. (*a*),(*c*) Instantaneous axial velocity and (*b*),(*d*) temperature contours in turbulent pipe flow as obtained from (*a*),(*b*) DNS-A and (*c*),(*d*) DNS-F. Thirty contours (from zero to the mean centreline value) are shown on a cross-stream plane and on a near-wall cylindrical shell ($y^+ \approx 15$), in colour scale from blue to red.

where $k_\phi = 2\pi/\lambda_\phi$ is the relevant wavenumber for the ϕ direction and x is the generic flow property. The axial velocity spectra clearly bring out a two-scale organisation of the flow field, with a near-wall peak associated with the wall regeneration cycle (Jiménez & Pinelli 1999), and an outer peak associated with outer-layer large-scale motions (Hutchins & Marusic 2007). The latter peak is found to be centred around $y/R \approx 0.3$, and to correspond to eddies with typical wavelength $\lambda_\phi \approx 1.5R$, consistent with that found by Ahn *et al.* (2015) for pipe flow at $Re_\tau = 3000$. Secondary peaks corresponding to harmonics of this fundamental wavelength are also observed here, suggesting that the typical outer modes are not purely sinusoidal with respect to the azimuthal direction. Notably, very similar organisation is found in the temperature field, the main difference being a somewhat broader peak at large wavelengths. Both the axial velocity and the temperature field exhibit a prominent spectral ridge corresponding to modes with typical azimuthal length scale $\lambda_\phi \sim y$, extending over about two decades, which can be interpreted as the footprint of a hierarchy of wall-attached eddies following Tonwsend's hypothesis (Townsend 1976).
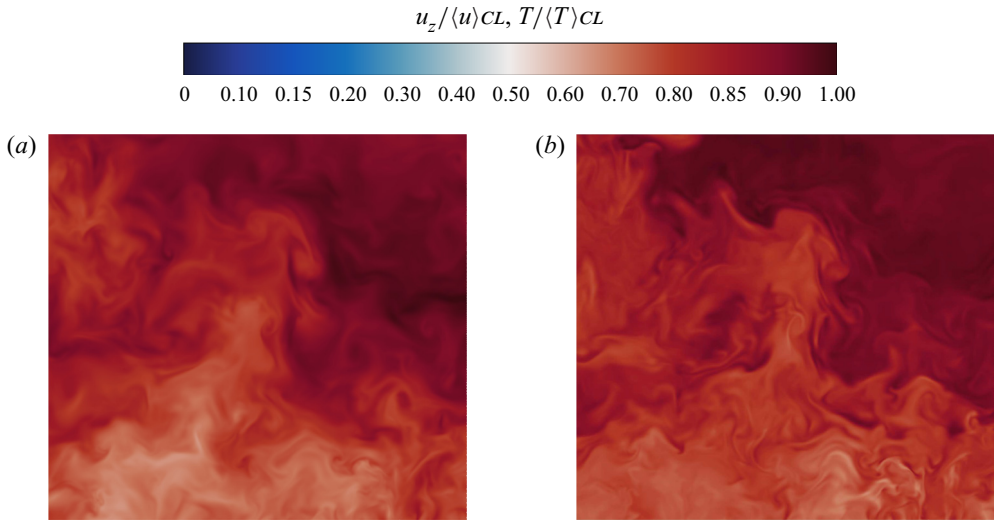
$$u_z/\langle u \rangle_{CL}, T/\langle T \rangle_{CL}$$

0   0.10 0.15 0.20 0.30 0.40 0.50 0.60 0.70 0.80 0.85 0.90 1.00

Figure 3. (*a*) Instantaneous axial velocity and (*b*) temperature contours in a subregion of the pipe cross section for DNS-F.
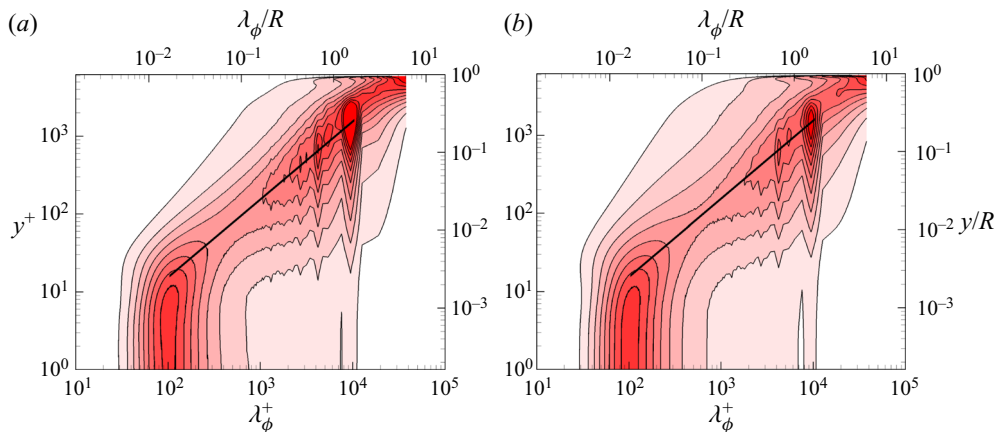

Figure 4. Variation of pre-multiplied, normalised azimuthal spectral densities of u_z ($\hat{E}_{u_z}$, (*a*)) and θ ($\hat{E}_\theta$, (*b*)) with wall distance, for flow case DNS-F. Wall distances and wavelengths are reported both in inner units (bottom, left), and in outer units (top, right). The solid diagonal line marks the trend $\lambda_\phi = 7.16y$. Contour levels from 0.05 to 0.5 are shown, in intervals of 0.05.

Hence, we may expect that inferences of the attached-eddy hypothesis regarding the behaviour of the axial velocity field also carry on to the temperature field.

Differences between velocity and scalar spectra are better scrutinised in figure 5, where we show spectral densities at a discrete set of wall distances. Figure 5(*a*) clearly brings out the bi-modal distribution of energy between the inner and the outer energetic sites. At intermediate wall distances ($y^+ \approx 100$) there is some mild evidence for a $\hat{E}_x \sim \lambda_\phi$ range which is also predicted from Townsend's theory (Nickels *et al.* 2005). Most importantly, the figure shows extra energy at small wavelengths in the temperature spectra, with exception of the nearest wall location. This difference is emphasised in figure 5(*b*), which shows spectra at $y/R = 0.3$ (at which the Taylor microscale Reynolds number is
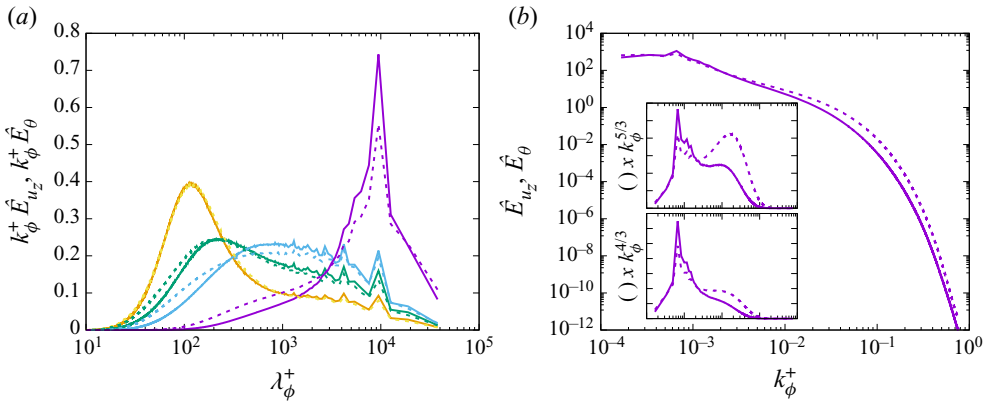
Figure 5. (*a*) Pre-multiplied, normalised spectral densities of u_z (solid) and θ (dashed), at $y^+ = 15$ (gold), $y^+ = 50$ (green), $y^+ = 100$ (cyan) and $y/R = 0.3$ (purple), for the DNS-F flow case. (*b*) Normalised spectral densities of u_z (solid) and θ (dashed) at $y/R = 0.3$, compensated by $k^{5/3}$ (top inset) and by $k^{4/3}$ (bottom inset).

$Re_\lambda \approx 400$) in the classical log–log, non-pre-multiplied representation. Whereas the u_z and θ spectra are very similar at the largest scales of motion, temperature tends to have a more shallow decay in the inertial and dissipative regions. This is well seen in the compensated representations shown in the insets. Whereas the classical $k^{-5/3}$ behaviour can be traced in the u_z spectra (at least in a tiny range of wavenumbers), the θ spectra seem to feature instead a $k^{-4/3}$ range, which is the theoretically expected behaviour for passive scalars in sheared turbulence (Lohse 1994).

Differences between axial velocity and temperature fields are also apparent in the close proximity of the wall. In figure 6 we show the probability density functions (p.d.f.s) for the wall-normal derivatives of u_z and θ. Both variables seem to tend to limit distributions in the infinite-Re limit, however whereas θ is mathematically bound to be positive, hence its wall-normal derivative must also be positive, u_z can have instantaneously negative values corresponding to local flow reversal. As a result, we find that the p.d.f. of the temperature gradient is well approximated by a log–normal distribution, as resulting from random multiplicative events. On the other hand, the p.d.f. of u_z obviously deviates from log–normality near the origin, but also its positive tail seems to be less prominent than for θ. The existence of local flow inversion at the wall, although with small probability (about 0.1 % overall) was noted in several previous studies (e.g. Lenaers *et al.* 2012), and related to the presence of oblique vortices inducing negative pressure fluctuations. This again corroborates the interpretation of different behaviour of u_z and θ as being due to the action of pressure.

3.2. *Mean temperature field*

The mean temperature profile in turbulent pipes has received extensive attention from theoretical and experimental studies, and the general consensus (Kader 1981) is that a logarithmic law well fits the experimental data. Recent studies have instead questioned the validity of the logarithmic law for the mean velocity field at finite Reynolds number (Jiménez & Moser 2007; Pirozzoli, Bernardini & Orlandi 2014; Lee & Moser 2015), and corrections to account for the effect of the core flow on the overlap layer have been proposed (e.g. Luchini 2017; Cantwell 2019; Monkewitz 2021). Such corrections mainly amount to addition of a linear term to the logarithmic profile which can be justified as a
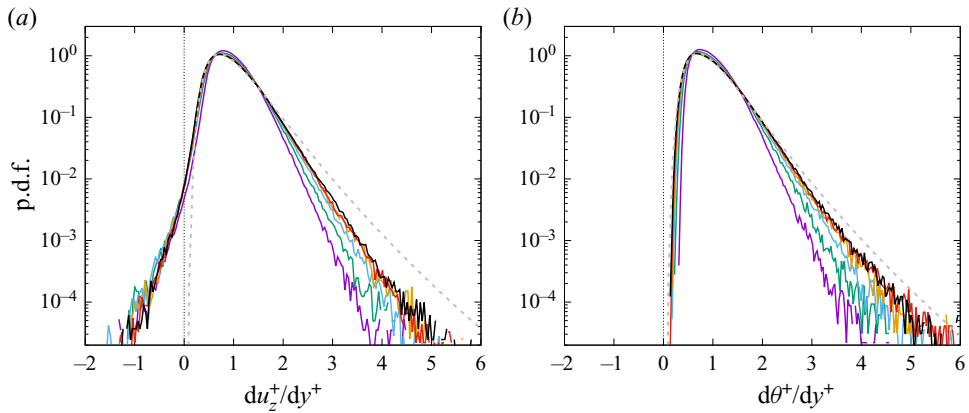
Figure 6. Probability density function of wall-normal derivatives of (*a*) axial velocity and (*b*) temperature. The colour codes are as in table 1. The dashed grey lines denote a log–normal distribution made to fit the DNS-F data.
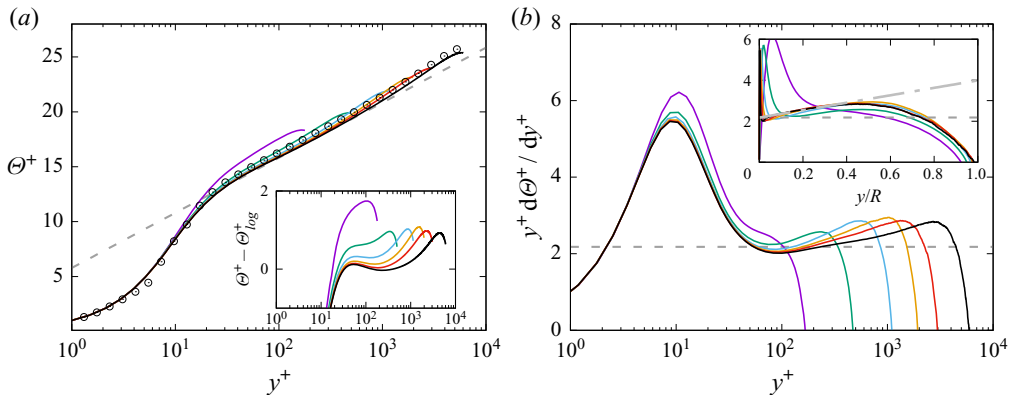

Figure 7. (*a*) Inner-scaled mean temperature profiles and (*b*) corresponding log-law diagnostic functions. Deviations from the assumed logarithmic wall law, $\Theta_{log}^+ = \log y^+/0.459 + 5.78$, are highlighted in the inset of (*a*). Circles denote the functional approximation proposed by Kader (1981), here evaluated for $Re_\tau = 6019$, $Pr = 1$. In (*b*), the dashed horizontal line denotes the inverse of the Kármán constant, $1/k_\theta$, and the dash-dotted lines in the inset denote the linear fit (3.3), with $k_\theta = 0.459$, $\alpha_\theta = 1.81$. See table 1 for colour codes.

higher-order term in the asymptotic matching between the inner and the outer layer (Afzal & Yajnik 1973), or as due to the presence of a mean pressure gradient in internal flows (Luchini 2017). Deviations of the profiles of passive scalars from the assumed logarithmic distribution were also observed in DNS of channel flow by Pirozzoli *et al.* (2016) and Alcántara-Ávila *et al.* (2021), amounting to a linear correction whose inner-scaled slope decreases with Re_τ. In figure 7, we show a series of temperature profiles computed with the present DNS, fitted with a logarithmic function with inverse slope $k_\theta = 0.459$, determined as described in the next section. The additive constant resulting from best fitting of the DNS data is $C_\theta \approx 5.78$. As shown in the inset of figure 7(*a*), the velocity profiles for $Re_\tau \geq 10^3$ follow this distribution with deviations smaller than 0.1 wall units from $y^+ \approx 30$ to $y/R \approx 0.1$. Hence, the standard log law is a good approximation of the temperature profile in the overlap layer for most practical purposes. The functional expression proposed by Kader (1981, (9), circles in panel (*a*)) is also found to provide

reasonable approximation of the data throughout the wall layer, even if with somewhat unnatural behaviour in the buffer layer and slight overprediction in the outer wall layer.

Very similar considerations apply to the mean axial velocity profiles (Pirozzoli *et al.* 2021, figure 3), which are visually well fitted with a logarithmic distribution, with estimated value of the von Kármán constant $k \approx 0.387$ (Pirozzoli *et al.* 2021), hence much less than k_θ, as consistently noted in previous studies on the subject. Based on the results presented in § 3.1, this difference can be justified by recalling that in the log layer (if present), $k/k_\theta \approx \nu_t/\alpha_t$, where ν_t and α_t are the turbulent kinematic and thermal diffusivities. As noted previously, the temperature field has a tendency to form sharper fronts, with steeper gradients, hence its effective diffusivity is expected to be larger than for the axial momentum. Accordingly, one may expect k to be smaller than k_θ, and the turbulent Prandtl number to be less than unity in the outer layer. More formal arguments to justify this difference, based on the properties of the similarity solution for the logarithmic mean profile over the inertial (non-diffusive) domain, were offered by Zhou, Klewicki & Pirozzoli (2019).

More detailed scrutiny about the behaviour of the mean temperature profile is carried out in figure 7(*b*), where we show the logarithmic diagnostic function,

$$\Xi_\theta = y^+ \, \mathrm{d}\Theta^+/\mathrm{d}y^+, \tag{3.2}$$

which is expected to be constant in the presence of a genuine logarithmic layer. As found previously for the axial velocity field (Pirozzoli *et al.* 2021, figure 4), no region with flat distribution of this indicator is, in fact, present. Rather, we note the occurrence of a nearly linear distribution from $y^+ \approx 100$ to $y/R \approx 0.4$, whose slope is approximately constant in outer units, hence the diagnostic function can be expressed as

$$\Xi_\theta \approx \frac{1}{k_\theta} + \alpha_\theta \frac{y}{R}, \tag{3.3}$$

with $\alpha_\theta \approx 1.81$. In other words, whereas a simple logarithmic profile is a reasonable approximation for engineering estimates, a linear correction yields significant improvement in the representation of the temperature profile, over a wider range of wall distances. Based on (3.3), a genuine log layer in the mean temperature profile would only emerge at infinite Reynolds number.

The structure of the core region of the flow is inspected in figure 8, where the mean temperature profiles are shown in defect form. Disregarding the DNS at the lowest Reynolds number (DNS-A and DNS-B) the scatter across the various temperature profiles for $y/R \geq 0.2$ is less than 1 %, which suggests that outer-layer similarity is very nearly achieved. As suggested by Pirozzoli (2014) and Orlandi, Bernardini & Pirozzoli (2015), the core velocity and temperature profiles can be closely approximated with simple universal quadratic distributions, which one can derive under the assumption of constant eddy diffusivity of momentum and temperature. In particular, we find that the formula

$$\Theta_{CL}^+ - \Theta^+ = C_O(1 - y/R)^2, \tag{3.4}$$

with $C_O = 5.5$, fits the mean temperature distribution in the pipe core quite well. Closer to the wall, the corrected logarithmic profile sets in at $y/R \lesssim 0.44$, here expressed in outer coordinates,

$$\Theta_{CL}^+ - \Theta^+ = -\frac{1}{k_\theta} \log(y/R) - \alpha_\theta \frac{y}{R} + B_\theta, \tag{3.5}$$

where data fitting yields $B_\theta = 0.732$. Although more elaborate descriptions of the outer velocity profiles are possible (e.g. Krug, Philip & Marusic 2017; Luchini 2018), the
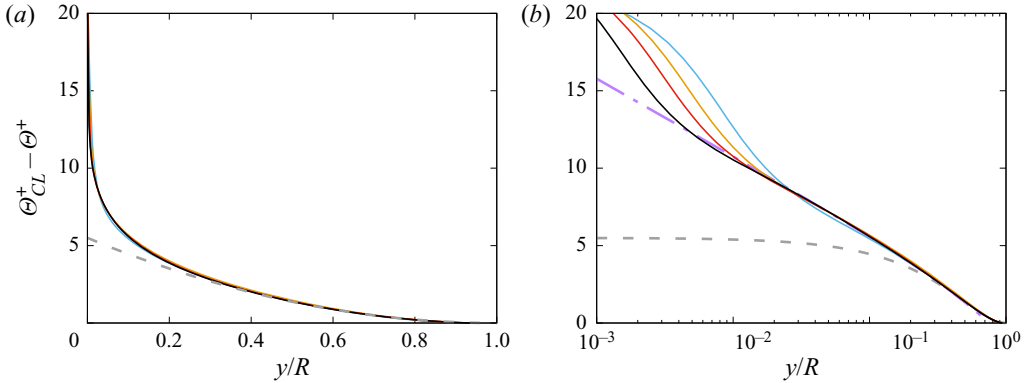
Figure 8. Mean defect temperature profiles in (*a*) linear and (*b*) semi-logarithmic scale. The dashed grey line marks a parabolic fit of the DNS data ($\Theta^+_{CL} - \Theta^+ = 5.5(1 - y/R)^2$) and the dot-dashed purple line in (*b*) the corrected outer-layer logarithmic fit $\Theta^+_{CL} - \Theta^+ = 0.732 - 1/0.459 \log(y/R) - 1.81(y/R)$. Only datasets DNS-C to DNS-F are shown here, see table 1 for colour codes.

composite profile compounding (3.4) and (3.5) yields accurate representation of the whole outer-layer mean temperature profile to within the scatter of the available DNS data.

3.3. *Heat transfer coefficients*

The primary subject of engineering interest in the study of passive scalar fields is the transfer coefficient at the wall, which can be expressed in terms of the Stanton number,

$$St = \frac{\alpha \left\langle \dfrac{dT}{dy} \right\rangle_w}{u_b(T_m - T_w)} = \frac{1}{u_b^+ \theta_m^+}, \tag{3.6}$$

where T_m is the mixed mean temperature (Kays *et al.* 1980),

$$T_m = 2 \int_0^R r\langle u_z\rangle\langle T\rangle dr \Big/ (u_b R^2), \tag{3.7}$$

with $\theta_m = (T_m - T_w)/T_\tau$ or, more frequently, in terms of the Nusselt number,

$$Nu = St\,Re_b\,Pr. \tag{3.8}$$

A predictive formula for the heat transfer coefficient in wall-bounded turbulent flows was derived by Kader & Yaglom (1972), based on the assumed existence of logarithmic layers for the mean velocity and temperature profiles as a function of the wall distance, and on universality of the core layer in defect representation. For the purpose of critically evaluating the assumptions made in the derivation of Kader's formula, we show (in figure 9) the distributions of the bulk and mean centreline values (namely, at $r = 0$) of velocity (figure 9*a*) and temperature (figure 9*b*), as a function of the friction Reynolds number, Consistently with theoretical expectations (e.g. Monkewitz 2021), the data suggest logarithmic increase of the bulk and centreline velocity with Re_τ according to

$$u_b^+ = \frac{1}{k} \log Re_\tau + B, \quad U_{CL}^+ = \frac{1}{k} \log Re_\tau + B_{CL}, \tag{3.9a,b}$$

with $k = 0.387$, $B = 1.229$ and $B_{CL} = 5.85$ (Pirozzoli *et al.* 2021). The relative standard deviation of the above formulae with respect to DNS data is approximately 0.2 % for u_b
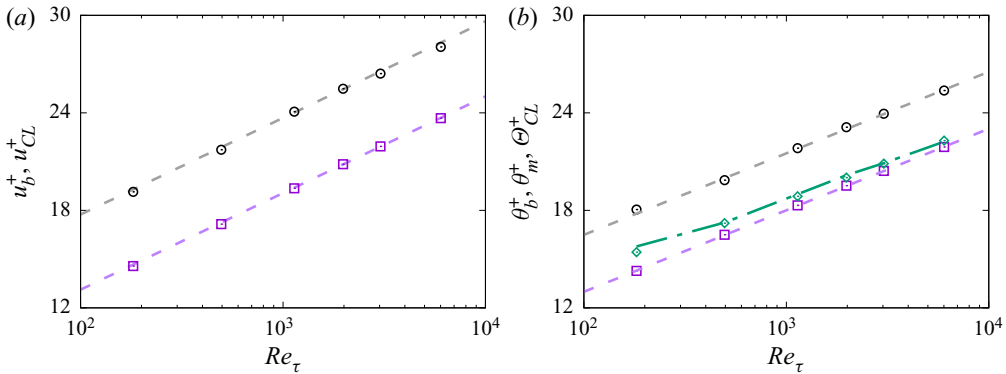
Figure 9. Bulk and centreline values of (*a*) axial velocity and (*b*) temperature. Bulk values (u_b^+, θ_b^+) are denoted with squares and centreline values (U_{CL}^+, Θ_{CL}^+) with circles. Diamonds in (*b*) denote the mixed mean temperature (θ_m^+). The dashed lines denote logarithmic fits of the DNS data. The dash-dotted line in (*b*) refers to the fit (3.11).

and 0.5 % for U_{CL}. Similar trends are here observed for the temperature field, which also exhibits logarithmic growth of the mean and centreline temperature with Re_τ, according to

$$\theta_b^+ = \frac{1}{k_\theta} \log Re_\tau + \beta, \quad \Theta_{CL}^+ = \frac{1}{k_\theta} \log Re_\tau + \beta_{CL}, \quad (3.10a,b)$$

with $\theta_b^+ = (T_b - T_w)/T_\tau$, and fit of the DNS data suggests $k_\theta = 0.459$, $\beta = 2.96$ and $\beta_{CL} = 6.46$. The relative standard deviation of the above formulae with respect to DNS data is approximately 0.06 % for θ_b and 0.5 % for Θ_{CL}, hence the quality of the fits is excellent as for the axial velocity field, and the resulting estimates of the flow constants, and especially of the scalar von Kármán constant appear to be quite robust.

Considering a large number of experimental works, Kader & Yaglom (1972) suggested $k_\theta \approx 0.47$, and provided empirical formulae for the additive constants as a function of the Prandtl number, $\beta(Pr) = 12.5Pr^{2/3} + 1/k_\theta \log Pr - 5.3$ and $\beta_{CL} = \beta + 0.6$. Studies carried out by means of DNS in planar channel flows with CHF show some scatter in the prediction of k_θ, likely due to low-Reynolds-number effects. For instance, Kawamura *et al.* (1999) reported $0.40 \leq k_\theta \leq 0.42$, Abe *et al.* (2004) reported $k_\theta \approx 0.43$, whereas more data at higher Reynolds number suggest $k_\theta \approx 0.44$ (Alcántara-Ávila *et al.* 2021). Studies carried out with CMT typically tend to yield slightly higher values, namely $k_\theta \approx 0.46$ (Pirozzoli *et al.* 2016), thus closer to Kader's prediction. It should be noted that all the above estimates were based on attempting to fit the temperature profiles with a logarithmic law, which as shown previously may not be a good approximation, especially at low Reynolds number. The method herein used to estimate the scalar von Kármán constant from the bulk and centreline temperatures yields greater accuracy and robustness, resulting in a value similar to that suggested by Kader & Yaglom (1972), and to values obtained using a similar approach, based on channel flow DNS data (Abe & Antonia 2017). It is also worth pointing out that the additive constants β, β_{CL} in (3.10a,b) do depend on the molecular Prandtl number (Kader & Yaglom 1972), hence the values herein reported are specific to the $Pr = 1$ case.

Determination of the appropriate Reynolds number trends of the mixed mean temperature is not as straightforward as for the bulk or the centreline temperature, because it involves integrating the product of the mean velocity and temperature distributions.

Simple developments (Kader & Yaglom 1972) suggest the expected behaviour to be

$$\theta_m^+ = \Theta_{CL}^+ - \beta_2 + \frac{\beta_3}{u_b^+}, \tag{3.11}$$

with β_2 and β_3 universal constants, hence, on account of (3.9a,b) and (3.10a,b), deviations from logarithmic dependence on Re_τ are to be expected. Figure 9 shows that it is indeed the case, and the mixed mean temperature (diamond symbols) seems to follow a near logarithmic distribution only at the highest Reynolds numbers under consideration. Values of the constants $\beta_2 = 4.92$, $\beta_3 = 39.6$, in (3.11) yield a fair fit of the DNS data. Although the scatter in the analytical fit (see the dash-dotted line) is more significant than for the other flow properties, this is clearly more accurate than a simple logarithmic fit. Corrections to the logarithmic law in the mixed mean temperature were generally disregarded in previous studies (Kader & Yaglom 1972; Abe & Antonia 2017), although they can be included in the analysis without additional difficulty.

Proceeding as proposed by Kader & Yaglom (1972), it is straightforward to derive a predictive formula for the inverse Stanton number,

$$\frac{1}{St} = \frac{k}{k_\theta} \frac{8}{\lambda} + \left(\beta_{CL} - \beta_2 - \frac{k}{k_\theta} B \right) \sqrt{\frac{8}{\lambda}} + \beta_3, \tag{3.12}$$

where the friction factor $\lambda = 8/u_b^{+2}$ can be obtained from (3.9a,b). Assuming strictly logarithmic variation of the mixed mean temperature with Re_τ (hence, setting $\beta_3 = 0$), Kader & Yaglom (1972) arrived at the following expression,

$$\frac{1}{St} = \frac{2.12 \log(Re_b \sqrt{\lambda/4}) + 12.5 Pr^{2/3} + 2.12 \log Pr - 10.1}{\sqrt{\lambda/8}}, \tag{3.13}$$

which could also be rearranged to a form more similar to (3.12). Additional correlations which are in wide use in the engineering practice were proposed by Gnielinski (1976),

$$Nu = \frac{Pr\lambda/8(Re_b - 1000)}{1 + 12.7(\lambda/8)^{1/2}(Pr^{2/3} - 1)}, \tag{3.14}$$

and by Kays *et al.* (1980),

$$Nu = 0.022 Re_b^{0.8} Pr^{0.5}. \tag{3.15}$$

Last, direct fitting of the DNS data (at $Pr = 1$) with a power-law expression yields

$$Nu = 0.0219 Re_b^{0.804}. \tag{3.16}$$

All the above predictive formulae are tested in figure 10, showing the predicted inverse Stanton number (figure 10a) and Nusselt number (figure 10b). With little surprise, we find that (3.12) with DNS-informed definition of the coefficients matches the DNS data quite well, with maximum relative error of 0.8 %. Despite minor differences in the coefficients with respect to the baseline predictive formula (3.15), the direct power-law fit given in (3.16) is also quite accurate, except at low Re_b. All other formulae fall short of the DNS data for St by up to 5 %. This difference may be partly due to inaccuracy of correlations based on old experimental data, to the fact that those are mainly tuned for the $Pr = 0.71$ case, whereas here $Pr = 1$, but also to the fact that the CMT setup herein used tends to slightly overpredict the heat flux as compared with the CHF approach (Abe & Antonia 2017; Alcántara-Ávila *et al.* 2021). It is interesting that differences are levelled off when
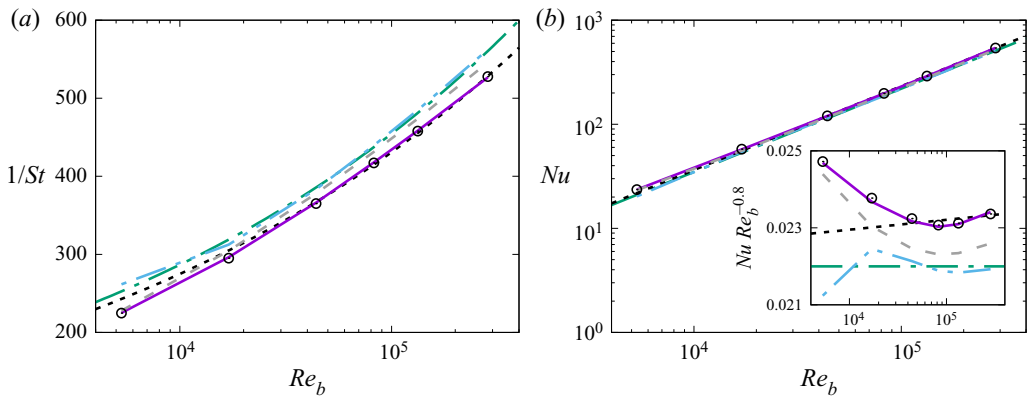
Figure 10. Distribution of (*a*) inverse Stanton number and (*b*) Nusselt number obtained from DNS (circles), and as predicted from (3.12) (solid line), from Kader's formula ((3.13), dashed), from the power-law data fit (3.16) (dotted), from Gnielinski analogy ((3.14), dot-dot-dashed) and from Kays–Crawford correlation ((3.15), dot-dashed). The inset in (*b*) shows the Nusselt number in compensated form ($Nu \times Re_b^{-0.8}$).

the popular representation in terms of the Nusselt number is used, as in figure 10(*b*). This suggests that the $1/St$ representation should be used when relatively small differences must be discriminated, or perhaps the compensated Nusselt representation used in the inset of figure 10(*b*).

3.4. *Temperature fluctuations statistics*

The distributions of the axial velocity and temperature variances are shown in figure 11, in inner scaling. All the profiles feature a prominent peak in the buffer layer at $y^+ \approx 15$, and an outer-layer shoulder which starts to form at sufficiently high Reynolds number. The most notable Reynolds number effect on the temperature variance profiles is sustained increase, as is the case of the axial velocity variance (Marusic & Monty 2019). According to Townsend's attached eddy model (Townsend 1976), growth of the wall-parallel velocity variances is expected to be logarithmic with Re_τ, on account of increased influence of 'distant' eddies. According to the spectral maps presented in figure 4, the attached-eddy hypothesis is also expected to apply to the temperature field. In fact, logarithmic growth of the peak temperature variance in turbulent planar channels was observed by Pirozzoli *et al.* (2016). This is confirmed by the present pipe DNS data, see figure 11(*b*), which compare the growth of the peak temperature variance with the axial velocity variance. Although the inferred growth rate is the same, the magnitude of the temperature variance peak is larger than for the axial velocity. This is the consequence (Pirozzoli *et al.* 2014) of near equality of the corresponding production terms in the buffer layer, however with extra energy draining in the axial velocity variance equation from the pressure term which tends to equalise kinetic energy across all the velocity components. No evidence is found based on the present data for saturation of the logarithmic growth, which has been inferred for the axial velocity variance in recent theoretical studies (Chen & Sreenivasan 2021).

The distributions of the turbulent heat flux, $\langle u_r \theta \rangle$, shown in figure 12, are visually indistinguishable from the corresponding turbulent shear stresses (reported with dashed lines). This is a further confirmation that the lift-up mechanism which is responsible for the establishment of correlation of u_z and θ with vertical velocity fluctuations, u_r, is nearly the same, and of essentially linear nature (Jiménez 2013). In both cases, the peak position grows approximately as the square root of Re_τ, corresponding to the minimal wall
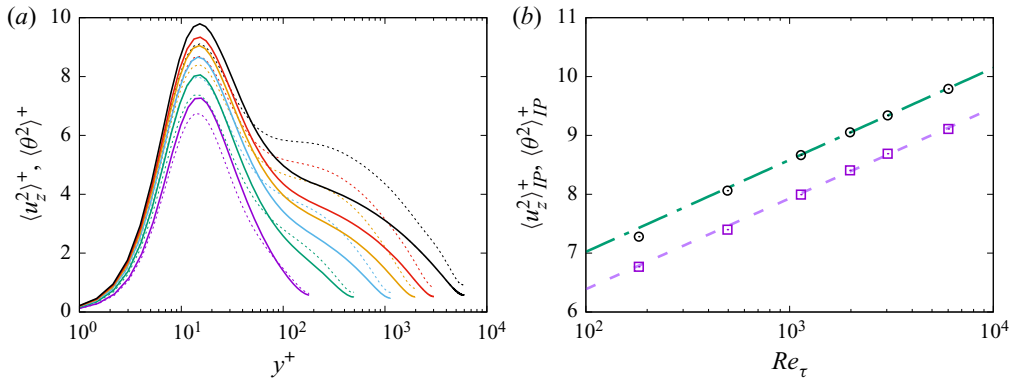
Figure 11. Distribution of (*a*) temperature variances and (*b*) corresponding peak value as a function of Re_τ. The dashed lines in (*a*) denote the distributions of the axial velocity variance. In (*b*), circles correspond to the peak temperature variance and squares to the peak axial velocity variance. Dash-dotted and dashed lines correspond to the associated logarithmic fits, namely $\langle \theta^2 \rangle_{IP}^+ = 0.68 \log Re_\tau + 3.9$, $\langle u_z^2 \rangle_{IP}^+ = 0.67 \log Re_\tau + 3.3$. Refer to table 1 for colour codes.
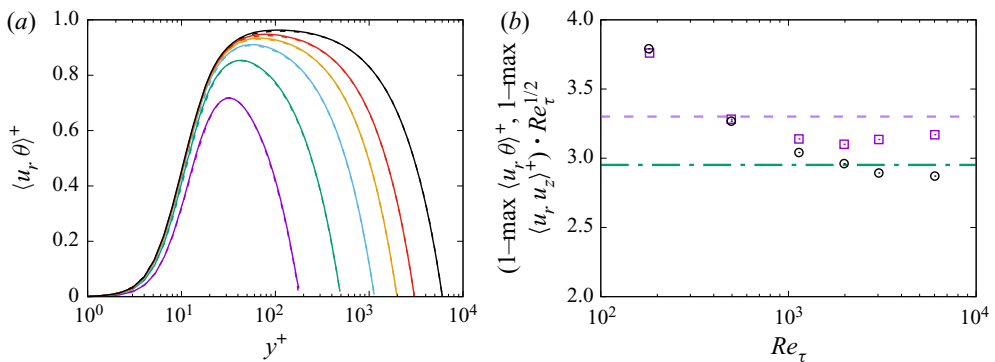

Figure 12. Distribution of (*a*) turbulent heat flux and (*b*) corresponding peak value (complement to one and premultiplied by $Re_\tau^{1/2}$) as a function of Re_τ. The dashed lines in (*a*) (barely visible) correspond to the distributions of the turbulent shear stress. In (*b*), circles correspond to the peak turbulent heat flux and squares to the peak turbulent shear stress. Dashed and dash-dotted lines correspond to the theoretical predictions (3.17) and (3.18), respectively. Refer to table 1 for colour codes.

distance for a logarithmic layer to develop (Klewicki, Fife & Wei 2009). Slight differences between the two distributions are nevertheless responsible for differences in the mean axial velocity and temperature profiles, on account on mean momentum balance and mean thermal balance (Saha *et al.* 2015; Zhou, Pirozzoli & Klewicki 2017). These differences are better appreciated in figure 12(*b*), where we show the peak turbulent heat flux and shear stress as a function of Re_τ. Based on mean momentum balance, and assuming the presence of a logarithmic layer (which is a bit inaccurate in view of what previously said), Orlandi *et al.* (2015) inferred that the peak turbulent shear stress should scale as

$$\max\langle u_r u_z \rangle \approx 1 - \frac{2}{\sqrt{kRe_\tau}}. \tag{3.17}$$

Similarly, it can be readily shown, based on mean thermal balance and assuming a log layer in the mean temperature distribution, that the peak turbulent heat flux should
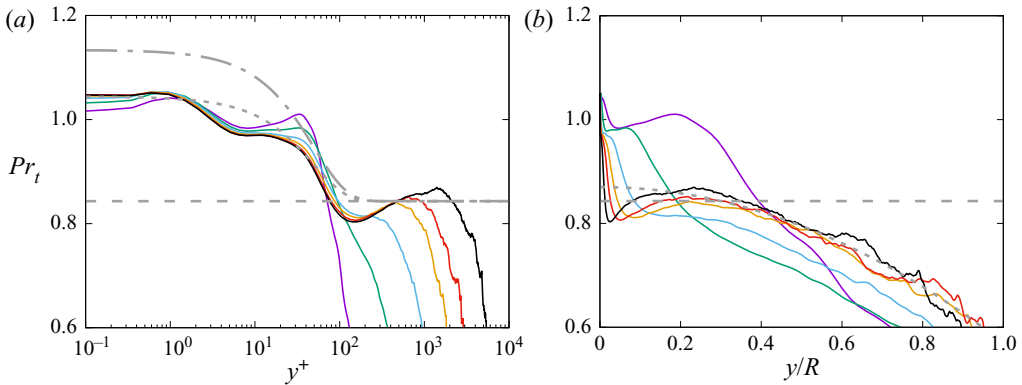
940 A45-16

Figure 13. Distribution of turbulent Prandtl number, in (*a*) inner and (*b*) outer coordinates. The dashed line denotes $Pr = k/k_\theta = 0.843$. In (*a*), the dash-dotted line denotes the prediction of (3.20) with the original set of constants and the dotted line the same formula, with $B = 32.2$. The dotted line in (*b*) denotes the fitting function (3.21). Refer to table 1 for colour codes.

scale as

$$\max\langle u_r\theta\rangle \approx 1 - \frac{2}{\sqrt{k_\theta Re_\tau}}. \tag{3.18}$$

These two trends are compared in figure 12(*b*). Whereas the data points coincide at low Reynolds number, some segregation is observed at the highest Reynolds numbers, at which the peaks tend to follow their respective theoretical distributions.

A quantity of great relevance in turbulence models of scalar transport is the turbulent Prandtl number, defined as (Cebeci & Bradshaw 1984)

$$Pr_t = \frac{\nu_t}{\alpha_t} = \frac{\langle u_r u_z\rangle}{\langle u_r\theta\rangle}\frac{\mathrm{d}\Theta/\mathrm{d}y}{\mathrm{d}U/\mathrm{d}y}, \tag{3.19}$$

whose distributions are shown in figure 13. As expected based on its definition, $Pr_t \approx k/k_\theta \approx 0.843$, through a large part of the outer layer, say from $y^+ \approx 100$ to $y/h \approx 0.25$. This is quite similar to what was found in channels (Pirozzoli *et al.* 2017; Alcántara-Ávila *et al.* 2021) and in general agreement with the values $Pr_t \approx 0.85$ suggested in reference publications (Kader 1981; Cebeci & Bradshaw 1984). Closer to the wall, the turbulent Prandtl number tends to exhibit a plateau with nearly unit value within the buffer layer ($5 \leq y^+ \leq 40$), as a result of the close similarity of the velocity and temperature fields in that region. At $y^+ \lesssim 1$ the eddy viscosity tends to exceed the eddy diffusivity, and as a consequence $Pr_t > 1$. Theoretical estimates for the near-wall behaviour of Pr_t were proposed by Cebeci (1973), based on a mixing length model with van Driest near-wall damping. This results in the estimate

$$Pr_t = \frac{k}{k_\theta}\frac{1 - \exp(-y^+/A)}{1 - \exp(-y^+/B)}, \tag{3.20}$$

where A and B are the damping functions for the velocity and scalar fields, respectively. The original choice of those two parameters, $A = 26$, $B = 34.96$ (for $Pr = 1$), captures the near-wall growth of Pr_t, although its value is overpredicted. Changing the damping constant for the temperature field to $B = 32.2$ (see the dotted grey line in figure 13*a*) improves the fit significantly, although the buffer-layer plateau is not captured. Regarding the outer layer, figure 13(*b*) seems to show tendency to universality in outer scaling at

940 A45-17

sufficiently high Reynolds number. As suggested by Rotta (1962) and Abe & Antonia (2017), the data are well fitted by a quadratic correlation, and we find

$$Pr_t = 0.87 - 0.3(y/R)^2, \tag{3.21}$$

for $y/R \gtrsim 0.25$.

4. Concluding comments

We have analysed the dynamics of passive scalars in turbulent pipe flow up to $Re_\tau \approx$ 6000, at unit Prandtl number. Compared with previous studies, the Reynolds number is sufficiently high here that the results are representative of realistic fully developed turbulence. A general expected finding, at least at $Pr = 1$, is that passive scalars exhibit a behaviour similar to the axial velocity field, being organised into streaks in the buffer layer and featuring low-wavenumber azimuthal modes in the bulk of the flow. The spectral maps also highlight close similarities at the large scales, which at the higher Reynolds number under study ($Re_\tau \approx 6000$), exhibit a prominent ridge with eddy size proportional to the wall distance, as suggested by Townsend's attached-eddy model. Besides overall similarity, differences are found as the passive scalar field has stronger tendency to form steep fronts, which are prevented in the velocity field by the action of pressure. Hence, scalar spectra tend to exhibit shallower $k^{-4/3}$ inertial range, for which the present DNS data provide convincing evidence.

Regarding the one-point statistics, we find that the mean scalar profiles in the overlap layer can be conveniently approximated by logarithmic distributions. However, significant improvement is obtained through addition of a linear corrective term scaling in outer units, which yields good fit of the data up to $y/R \approx 0.44$. Further away from the wall, the mean scalar profile is approximated with excellent accuracy by a simple quadratic distribution. Notable differences are found in the von Kármán constants, which we estimate to be $k_\theta \approx$ 0.459 for the scalar field, and $k \approx 0.387$ for the axial velocity field, which we obtain by fitting the trends of the respective bulk values with the friction Reynolds number, with estimated error much less than 1 %. The DNS data help explaining this difference as the result of greater effective diffusivity of the scalar field resulting from the formation of smaller scales. Reynolds number effects are apparent in the distributions of the passive scalar variance, which show sustained logarithmic growth of the inner peak magnitude, as after Townsend's attached-eddy hypothesis. No evidence for saturation of this growth is found, at the Reynolds numbers under scrutiny. Notably, the growth rate is found to be very nearly the same as for the axial velocity variance.

Full insight into the scalar and velocity statistics provided by DNS allows to pinpoint possible limitations of classical analyses of heat transfer in smooth pipes and of classical modelling assumptions for passive scalar transport. In particular, whereas logarithmic dependence of the mixed mean temperature over Re_τ was assumed by Kader (1981), we find that finite-Re deviations should be accounted for, thus obtaining the predictive formula (3.12), which is found to be more accurate than the classical Kader's formula (3.13). It is noteworthy that deviations of empirical formulae employed in the engineering practice are sometimes hidden in the traditional Nu versus Re_b representation, whereas they show up much more clearly when the inverse Stanton number is reported, as in figure 10(*a*). Regarding the distributions of the turbulent Prandtl number, which is needed for turbulence modelling, the DNS data show that in the overlap layer the assumption $Pr_t \approx 0.843$ is quite appropriate. However, significant deviations are found farther from the wall, with quadratic decrement with the wall distance. Deviations are also

found in the near-wall region, where Pr_t exceeds unity. This fact is roughly acknowledged in existing engineering correlations (Cebeci 1973; Kays *et al.* 1980), but the accuracy is far from acceptable. Whereas the above-noted shortcoming of common modelling assumptions and predictive formulae may be minor to be appreciated in practical contexts, as may be related with the assumed unit Prandtl number, with the particular form of volumetric heating used as forcing and with assumed isothermal wall, the procedure herein outlined nevertheless serves to illustrate a general use of DNS as a way for testing hypotheses in more general situations, for instance at higher Prandtl number, at which the thermal boundary layer is thinner than the kinematic one.

A natural extension of the present study would be, in fact, considering the case of lower and higher Prandtl numbers, which we could not include in the present DNS owing to memory restrictions. That would allow to verify the Prandtl number dependence of the β_{CL} constant in the main predictive equation for the heat transfer (3.12). Equally interesting would be carrying out the present DNS within the CHF approach, whereby strictly constant heat flux is retained in time. That would allow the reasons for the small (but sizeable) deviations observed in figure 10 to be elucidated with respect to engineering correlations in current use.

Author ORCIDs.
- Sergio Pirozzoli https://orcid.org/0000-0002-7160-3023;
- Roberto Verzicco https://orcid.org/0000-0002-2690-9998;
- Paolo Orlandi https://orcid.org/0000-0002-0305-5723.

REFERENCES

ABE, H. & ANTONIA, R.A. 2009 Near-wall similarity between velocity and scalar fluctuations in a turbulent channel flow. *Phys. Fluids* **21**, 025109.

ABE, H. & ANTONIA, R.A. 2017 Relationship between the heat transfer law and the scalar dissipation function in a turbulent channel flow. *J. Fluid Mech.* **830**, 300–325.

ABE, H., KAWAMURA, H. & MATSUO, Y. 2004 Surface heat-flux fluctuations in a turbulent channel flow up to $Re_\tau = 1020$ with $Pr = 0.025$ and 0.71. *Intl J. Heat Fluid Flow* **25**, 404–419.

AFZAL, N. & YAJNIK, K. 1973 Analysis of turbulent pipe and channel flows at moderately large Reynolds number. *J. Fluid Mech.* **61**, 23–31.

AHN, J., LEE, J.H., LEE, J., KANG, J.-H. & SUNG, H.J. 2015 Direct numerical simulation of a 30R long turbulent pipe flow at $Re_\tau = 3000$. *Phys. Fluids* **27**, 065110.

AKSELVOLL, K. & MOIN, P. 1996 An efficient method for temporal integration of the Navier–Stokes equations in confined axisymmetric geometries. *J. Comput. Phys.* **125**, 454–463.

ALCÁNTARA-ÁVILA, F., HOYAS, S. & PÉREZ-QUILES, M.J. 2018 DNS of thermal channel flow up to $Re\tau = 2000$ for medium to low Prandtl numbers. *Intl J. Heat Mass Transfer* **127**, 349–361.

ALCÁNTARA-ÁVILA, F., HOYAS, S. & PÉREZ-QUILES, M.J. 2021 Direct numerical simulation of thermal channel flow for $Re\tau = 5000$ and $Pr = 0.71$. *J. Fluid Mech.* **916**, A29.

ANTORANZ, A., GONZALO, A., FLORES, O. & GARCIA-VILLALBA, M. 2015 Numerical simulation of heat transfer in a pipe with non-homogeneous thermal boundary conditions. *Intl J. Heat Fluid Flow* **55**, 45–51.

CANTWELL, B.J. 2019 A universal velocity profile for smooth wall pipe flow. *J. Fluid Mech.* **878**, 834–874.

CEBECI, T. 1973 A model for eddy conductivity and turbulent Prandtl number. *J. Heat Transfer* **95**, 227–234.

CEBECI, T. & BRADSHAW, P. 1984 *Physical and Computational Aspects of Convective Heat Transfer*. Springer-Verlag.

CHEN, X. & SREENIVASAN, K.R. 2021 Reynolds number scaling of the peak turbulence intensity in wall flows. *J. Fluid Mech.* **908**, R3.

GNIELINSKI, V. 1976 New equations for heat and mass transfer in turbulent pipe and channel flow. *Intl Chem. Engng* **16**, 359–367.

GOWEN, R.A. & SMITH, J.W. 1967 The effect of the Prandtl number on temperature profiles for heat transfer in turbulent pipe flow. *Chem. Engng Sci.* **22**, 1701–1711.

HARLOW, F.H. & WELCH, J.E. 1965 Numerical calculation of time-dependent viscous incompressible flow of fluid with free surface. *Phys. Fluids* **8**, 2182–2189.

HOYAS, S. & JIMÉNEZ, J. 2006 Scaling of velocity fluctuations in turbulent channels up to $Re_\tau = 2003$. *Phys. Fluids* **18**, 011702.

HUTCHINS, N. & MARUSIC, I. 2007 Evidence of very long meandering features in the logarithmic region of turbulent boundary layers. *J. Fluid Mech.* **579**, 1–28.

JIMÉNEZ, J. 2013 How linear is wall-bounded turbulence? *Phys. Fluids* **25** (11), 110814.

JIMÉNEZ, J. 2018 Coherent structures in wall-bounded turbulence. *J. Fluid Mech.* **842**, P1.

JIMÉNEZ, J. & MOSER, R.D. 2007 What are we learning from simulating wall turbulence? *Phil. Trans. R. Soc. Lond.* A **365**, 715–732.

JIMÉNEZ, J. & PINELLI, A. 1999 The autonomous cycle of near-wall turbulence. *J. Fluid Mech.* **389**, 335–359.

KADER, B.A. 1981 Temperature and concentration profiles in fully turbulent boundary layers. *Intl J. Heat Mass Transfer* **24**, 1541–1544.

KADER, B.A. & YAGLOM, A.M. 1972 Heat and mass transfer laws for fully turbulent wall flows. *Intl J. Heat Mass Transfer* **15** (12), 2329–2351.

KAWAMURA, H., ABE, H. & MATSUO, Y. 1999 DNS of turbulent heat transfer in channel flow with respect to Reynolds and Prandtl number effects. *Intl J. Heat Fluid Flow* **20**, 196–207.

KAYS, W.M., CRAWFORD, M.E. & WEIGAND, B. 1980 *Convective Heat and Mass Transfer*. McGraw-Hill.

KIM, J. & MOIN, P. 1985 Application of a fractional-step method to incompressible Navier–Stokes equations. *J. Comput. Phys.* **59**, 308–323.

KIM, J. & MOIN, P. 1989 Transport of passive scalars in a turbulent channel flow. In *Turbulent Shear Flows*, vol. 6, pp. 85–96. Springer.

KLEWICKI, J., FIFE, P. & WEI, T. 2009 On the logarithmic mean profile. *J. Fluid Mech.* **638**, 73–93.

KRUG, D., PHILIP, J. & MARUSIC, I. 2017 Revisiting the law of the wake in wall turbulence. *J. Fluid Mech.* **811**, 421–435.

LEE, M. & MOSER, R.D. 2015 Direct simulation of turbulent channel flow layer up to $Re_\tau = 5200$. *J. Fluid Mech.* **774**, 395–415.

LENAERS, P., LI, Q., BRETHOUWER, G., SCHLATTER, P. & ÖRLÜ, R. 2012 Rare backflow and extreme wall-normal velocity fluctuations in near-wall turbulence. *Phys. Fluids* **24**, 035110.

LOHSE, D. 1994 Temperature spectra in shear flow and thermal convection. *Phys. Lett.* A **196**, 70–75.

LUCHINI, P. 2017 Universality of the turbulent velocity profile. *Phys. Rev. Lett.* **118** (22), 224501.

LUCHINI, P. 2018 Structure and interpolation of the turbulent velocity profile in parallel flow. *Eur. J. Mech. (B/Fluids)* **71**, 15–34.

MARUSIC, I. & MONTY, J.P. 2019 Attached eddy model of wall turbulence. *Annu. Rev. Fluid Mech.* **51**, 49–74.

MOIN, P. & VERZICCO, R. 2016 On the suitability of second-order accurate discretizations for turbulent flow simulations. *Eur. J. Mech. (B/Fluids)* **55**, 242–245.

MONIN, A.S. & YAGLOM, A.M. 1971 *Statistical Fluid Mechanics: Mechanics of Turbulence*, vol. 1. MIT Press.

MONKEWITZ, P.A. 2021 The late start of the mean velocity overlap log law at $y^+ = O(10^3)$ – a generic feature of turbulent wall layers in ducts. *J. Fluid Mech.* **910**, A45.

NAGANO, Y. & TAGAWA, M. 1988 Statistical characteristics of wall turbulence with a passive scalar. *J. Fluid Mech.* **196**, 157–185.

NICKELS, T.B., MARUSIC, I., HAFEZ, S.M. & CHONG, M.S. 2005 Evidence of the k^{-1} law in a high-Reynolds-number turbulent boundary layer. *Phys. Rev. Lett.* **95**, 074501.

ORLANDI, P., BERNARDINI, M. & PIROZZOLI, S. 2015 Poiseuille and Couette flows in the transitional and fully turbulent regime. *J. Fluid Mech.* **770**, 424–441.

ORLANDI, P. & FATICA, M. 1997 Direct simulations of turbulent flow in a pipe rotating about its axis. *J. Fluid Mech.* **343**, 43–72.

PILLER, M. 2005 Direct numerical simulation of turbulent forced convection in a pipe. *Intl J. Numer. Meth. Fluids* **49** (6), 583–602.

PIROZZOLI, S. 2014 Revisiting the mixing-length hypothesis in the outer part of turbulent wall layers: mean flow and wall friction. *J. Fluid Mech.* **745**, 378–397.

PIROZZOLI, S., BERNARDINI, M. & ORLANDI, P. 2014 Turbulence statistics in Couette flow at high Reynolds number. *J. Fluid Mech.* **758**, 327–343.

PIROZZOLI, S., BERNARDINI, M. & ORLANDI, P. 2016 Passive scalars in turbulent channel flow at high Reynolds number. *J. Fluid Mech.* **788**, 614–639.

PIROZZOLI, S., BERNARDINI, M., VERZICCO, R. & ORLANDI, P. 2017 Mixed convection in turbulent channels with unstable stratification. *J. Fluid Mech.* **821**, 482–516.

PIROZZOLI, S. & ORLANDI, P. 2021 Natural grid stretching for DNS of wall-bounded flows. *J. Comput. Phys.* **439**, 110408.

PIROZZOLI, S., ROMERO, J., FATICA, M., VERZICCO, R. & ORLANDI, P. 2021 One-point statistics for turbulent pipe flow up to $Re_\tau \approx 6000$. *J. Fluid Mech.* **926**, A28.

REDJEM-SAAD, L., OULD-ROUISS, M. & LAURIAT, G. 2007 Direct numerical simulation of turbulent heat transfer in pipe flows: effect of Prandtl number. *Intl J. Heat Fluid Flow* **28** (5), 847–861.

ROTTA, J.C. 1962 Turbulent boundary layers in incompressible flow. *Prog. Aerosp. Sci.* **2** (1), 1–95.

RUETSCH, G. & FATICA, M. 2014 *CUDA Fortran for Scientists and Engineers*. Elsevier.

RUSSO, S. & LUCHINI, P. 2017 A fast algorithm for the estimation of statistical error in DNS (or experimental) time averages. *J. Comput. Phys.* **347**, 328–340.

SAHA, S., CHIN, C., BLACKBURN, H.M. & OOI, A.S.H. 2011 The influence of pipe length on thermal statistics computed from dns of turbulent heat transfer. *Intl J. Heat Fluid Flow* **32** (6), 1083–1097.

SAHA, S., KLEWICKI, J.C., OOI, A.S.H. & BLACKBURN, H.M. 2015 Comparison of thermal scaling properties between turbulent pipe and channel flows via DNS. *Intl J. Therm. Sci.* **89**, 43–57.

STEVENS, R.J.A.M., VAN DER POEL, E.P., GROSSMANN, S. & LOHSE, D. 2013 The unifying theory of scaling in thermal convection: the updated prefactors. *J. Fluid Mech.* **730**, 295–308.

STRAUB, S., FOROOGHI, P., MAROCCO, L., WETZEL, T. & FROHNAPFEL, B. 2019 Azimuthally inhomogeneous thermal boundary conditions in turbulent forced convection pipe flow for low to medium Prandtl numbers. *Intl J. Heat Fluid Flow* **77**, 352–358.

SUBRAMANIAN, C.S. & ANTONIA, R.A. 1981 Effect of Reynolds number on a slightly heated turbulent boundary layer. *Intl J. Heat Mass Transfer* **24**, 1833–1846.

TOWNSEND, A.A. 1976 *The Structure of Turbulent Shear Flow*, 2nd edn. Cambridge University Press.

VERZICCO, R. & ORLANDI, P. 1996 A finite-difference scheme for three-dimensional incompressible flows in cylindrical coordinates. *J. Comput. Phys.* **123**, 402–414.

WU, X. & MOIN, P. 2008 A direct numerical simulation study on the mean velocity characteristics in turbulent pipe flow. *J. Fluid Mech.* **608**, 81–112.

ZHOU, A., KLEWICKI, J. & PIROZZOLI, S. 2019 Properties of the scalar variance transport equation in turbulent channel flow. *Phys. Rev. Fluids* **4** (2), 024606.

ZHOU, A., PIROZZOLI, S. & KLEWICKI, J. 2017 Mean equation based scaling analysis of fully-developed turbulent channel flow with uniform heat generation. *Intl J. Heat Mass Transfer* **115**, 50–61.